Applicability and Performance of Standard Compression Methods for Efficient Data Transmission and Storage in Radar Networks

GEORG KÖRNER [1], MARCEL HOFFMANN [1] (Student Member, IEEE), PATRICK STIEF [1], MENGYU ZHANG [1], RAINER RÜCKERT[1], CHRISTIAN HERGLOTZ [2] (Member, IEEE), ANDRÉ KAUP [2] (Fellow, IEEE), AND MARTIN VOSSIEK [1] (Fellow, IEEE)

(Regular Paper)

[1]Institute of Microwaves and Photonics, Friedrich-Alexander-Universität Erlangen-Nürnberg (FAU), 91058 Erlangen, Germany
[2]Multimedia Communications and Signal Processing, Friedrich-Alexander-Universität Erlangen-Nürnberg (FAU), 91058 Erlangen, Germany

CORRESPONDING AUTHOR: Georg Körner (e-mail: georg.gk.koerner@fau.de).

ABSTRACT Modern sensor networks—those used for autonomous driving, security systems, human motion tracking, or smart city/smart factory applications—are shifting to a more centralized data processing approach to enable efficient multimodal sensor fusion for optimal environment perception in complex dynamic situations. Among lidars and cameras, radars are typical for these applications, but they generate huge amounts of data, which cannot be transmitted or stored effectively in current setups. Consequently, manufacturers usually have to process the data "on sensor." This results in transmitting only a few extracted features as point clouds or object lists to a central processing unit, which usually causes a significant loss of information. With this approach, advanced processing—such as enhancement of resolution by coherent combination of sensors or ghost target removal with advanced algorithms—is hardly possible. To overcome this, we suggest an alternative method by using signal-based compression with defined losses. The following topology will be proposed: the sensors encode raw data without prior radar-specific processing and after transmission, a central unit decodes and processes the radar data, thus benefiting from its more powerful heterogeneous processing system. We will analyze lossless compression algorithms with rate savings of about 30% to 65%, but the focus is on lossy compression algorithms that incorporate higher compression ratios by allowing negligible errors. It is shown that state-of-the-art multimedia compression algorithms can obtain rate savings of 99%, and radar specific algorithms can add a 50-fold gain on top, reaching 99.98%. To assess the distortions of compressed data, we then present different radar-specific evaluation metrics.

INDEX TERMS Radar, FMCW radar, OFDM modulation, data compression, source coding.

I. INTRODUCTION

Radar-based monitoring of the environment has gained increasing attention over the last decade because these systems provide a very robust way of detecting and mapping three-dimensional (3D) objects. Surveillance [1], geological [2], medical [3], and automotive applications are only a fraction of cases in which radars are used [4]. Automotive applications in particular are a driving factor for the development of new radar systems and technology [5]. Today, cars detect objects in their surroundings with multiple radar sensors for different applications (See Fig. 1). Each radar sensor processes the received data and sends features via the "slow" vehicular network to a central processing unit, which then fuses the data from different radars and other sensors [6]. This fusion enables a precise and enhanced understanding of the vehicle's environment and is a key factor to the development of autonomous driving. Furthermore, in self-driving applications, there may be the legal necessity to store data for insight into
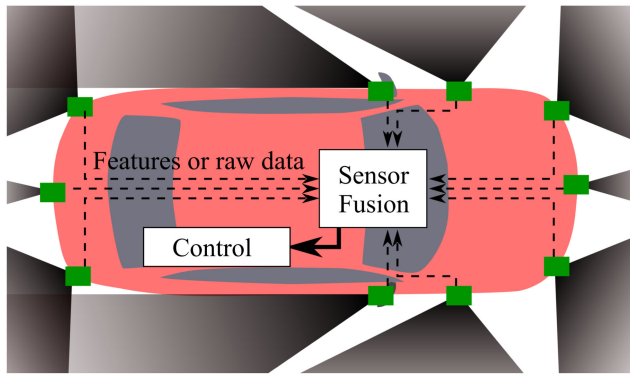
FIGURE 1. Visual depiction of a possible radar setup in cars [8], [9]. The radar modules (green) are responsible for analog signal conditioning. Processed point cloud features or raw data are sent to a central processing unit, which fuses the point clouds or raw data and can control the movement of the car.

FIGURE 2. Processing steps for automotive (FMCW) radar applications according to [15]. State-of-the-art vehicular radar systems with processing in the individual radar modules are depicted in black in (a). The proposed, centralized data processing setup is colored red in (b).

the causes of accidents. Storing (and replaying) data in remote data centers is also required for the training of future artificial intelligence (AI) applications for failsafe autonomous driving [7].

Moreover, the current processing chain discards much information obtained by the radar. The data are typically processed on the radar module itself, and multiple features are extracted from the processed radar cubes and stored in object lists or point clouds. With these, the vehicle's surroundings can be represented in an amplitude or occupancy grid map [10]. However, there are various disadvantages to this approach. First, a target's shape, as well as any information on the Doppler signature, is lost. Second, shadowed targets with low power are treated as noise and are therefore not considered in the point clouds. However, this information is required to enable or improve object classification [3]. Third, the inability to combine different radar sensors through coherent processing for improved resolution and ghost target suppression [11] is a lost potential of feature lists. Fourth, the maximum information can be obtainable if the data of different sensor types–for e.g., navigation systems, inertial measurement unit, camera, lidar, and radar–are combined at the raw-data level in a central processing unit.

Radar sensors have many shapes and working principles. The radar sensors of a car can be characterized by detection parameters, such as precision and maximum range, or by derived technical parameters such as bandwidth, signal-to-noise ratio (SNR), or others. There are short-range radars for pedestrian detection and city driving that require high precision but no large maximum distance. To fulfill their purposes, they need to incorporate a large bandwidth and antenna arrays with many antennas. Meanwhile, there are long-range radars for lane keeping and adaptive cruise control, which only need a small antenna beam width to separate the relevant parts of a street. Besides the different applications, most radars these days use frequency modulated continuous wave (FMCW) [12] chirp sequence schemes. Other emerging radar systems use
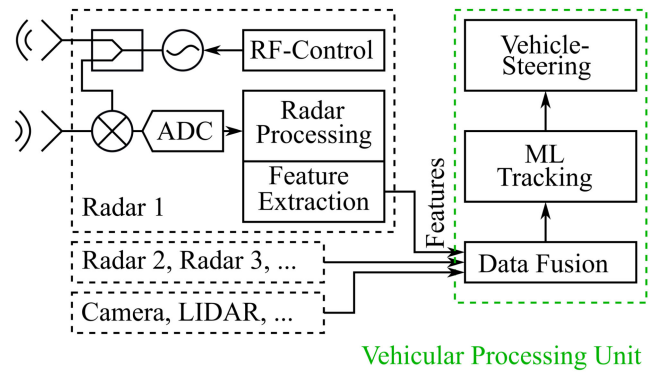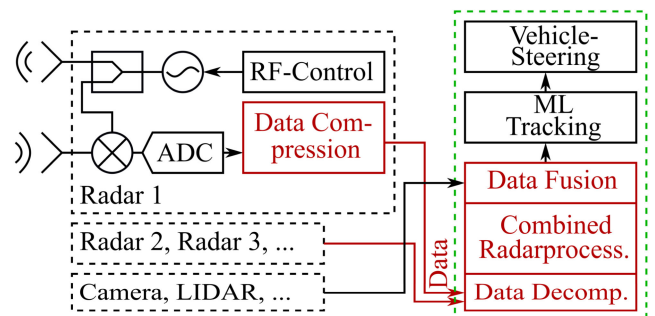
stepped frequency continuous wave (SFCW) [13] or orthogonal frequency division multiplexing (OFDM) [14]. These are very different modulations, but within their individual signal processing chain, the data's representation is very similar. In this paper, we will define common properties and show that all of them can be compressed.

Fig. 2(a) shows a typical FMCW-radar module in an automotive environment with the relevant processing steps. State-of-the-art modules are responsible for radio frequency (RF) generation and control, radar processing, and feature extraction, all final radar processing steps.

In the proposed setup in Fig. 2(b), the processing steps are replaced by a generic compression algorithm, which can be accelerated by dedicated hardware. The designated processing unit ("On" or "Off"-Vehicle) then decompresses this data and applies the advanced or combined processing and fusions them with other sensors for generation of the output features. Through this process, the vehicular processing system has instant access to data from all radar modules. Additionally, this processing unit has fewer restrictions in terms of power consumption or computational power than the radar sensors at their exposed installation position. In this step, the compressed data can easily be simultaneously stored for both
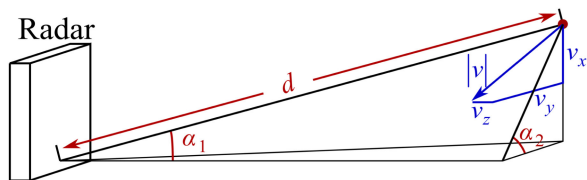
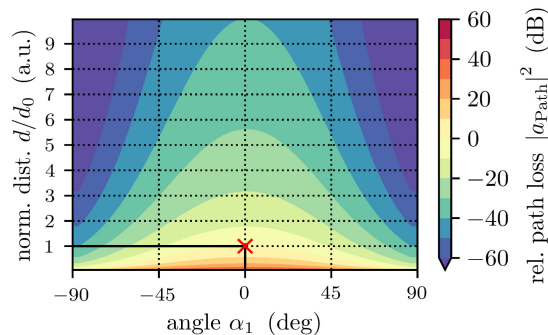**FIGURE 3.** Point target model used for the simulation. All the parameters are generated by random processes.

FIGURE 4. Relative receiving power $|a_{Path}|^2$ referenced from the normalized distance at 0°, marked by the red x. As can be seen, the amplitudes decrease steadily, even on a logarithmic scale. The antenna pattern used is that of the patch antenna derived from the antenna pattern of the 77GHz Frontend for the "Inras Radarbook" [18].

accident reconstruction and improvement of AI in research environments.

This paper begins with a short introduction to the underlying point target signal models with which the simulated data are generated. This is done to show the possibilities of data compression. Subsequently, metrics for classifying the quality of the lossy compression algorithms are developed and depicted. The main section will show the application of these signal models to different multimedia compression algorithms. Additionally, a simple, radar-processing inspired algorithm that fuses on discrete Fourier transform (DFT) for lossy compression is presented. The last section confirms the theoretical results by analyzing real-world measurements.

II. POINT TARGET MODEL

The data model is depicted here to illustrate the reasons for the expected beneficial compression ratios. The radar scenery is represented in a simplified manner using point targets with a distance d and direction angles α_1 and α_2 from which they are perceived.

Moreover, we used this point target model to simulate data of a radar system that also covers realistic worst-case scenarios. The parameters for each scene were chosen in such a manner that they are as diverse as possible, and the signals used the full range of the samples perfectly. In most realistic scenes, targets mostly have the same velocity or are only perceived from limited directions. We do not want to limit the compression algorithm to such scenes. Here, the model was not only used for signal generation, but also for providing a "ground truth," which is used further for evaluating the different compression algorithms. In this context, without understanding the true underlying scenery and its reflectivity, it would not be possible to distinguish between relevant data and noise-dominated parts. Thus, with a simulation like this, the uncertainties of real scenes are tackled.

Fig. 3 shows the relevant geometric parameters for a single target. The statistical parameters are as follows:

- A log-normal distributed random variable was used for the distance d. This is chosen because targets in the front shadow others behind them. Such multiplicative behavior leads to a log-normal distribution. These processes are used in similar applications in geographic science [16].
- The angle α_1. between the distance vector and the surface normal of the radar was chosen, as this angle is

highly influenced by the antenna pattern. The value was chosen to be uniformly distributed from −90° to 90° since there are no targets expected from behind the radar, and there is an equal probability of all angles.

- The angle α_2 was also uniformly distributed from −90° to 90° since there is no distinct direction of expected targets.
- The velocity components of the targets $v_x v_y$ and v_z were also chosen in such a way that they are uniformly distributed. The maxima of these properties were chosen, so that the maximum absolute velocity $|v|$ is alias free in any direction for the chosen radar parameters.

The radar equation [17] is used for the attenuation of each path for each individual combination of antennas. The power attenuation $|a_{Path}|^2$ is defined as

$$\left|a_{Path}\right|^2 (d(t)) = \frac{G_{Tx}(\omega) \cdot G_{Rx}(\omega) \cdot \sigma(\omega) \cdot \lambda(\omega)^2}{(4\pi)^3 \cdot d(t)^4}. \quad (1)$$

Here, the radar cross-section σ of the target is considered constant for all targets. The wavelength λ is also approximated as constant since the bandwidth is small compared to the absolute frequency. The transfer functions of the transmit G_{Tx} and receive path G_{Rx} are considered to only be dependent on the receiving and transmitting antenna patterns, which are simplified as having the same patterns G_{An}. However, the absolute values are not of importance here since they can be changed in a large range by amplification and attenuation within the signaling chain and in conversion. Therefore, we use the following proportional representation for the simulation of the attenuated signals:

$$\left|a_{Path}\right|^2 (d, \alpha_1) \propto \frac{G_{An}(\alpha_1)^2}{d(t)^4}. \quad (2)$$

The relative path losses $|a_{Path}^2|$ are visualized in Fig. 4. With these assumptions, it becomes obvious that for increasing distances d and large angles α_1, the amplitudes largely decrease. Meanwhile, for high velocities $|v|$, the possibilities of a target decrease largely since only the effective component
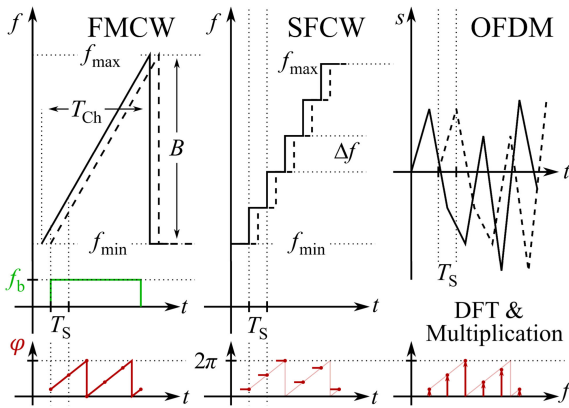
FIGURE 5. Waveforms for transmitted (bold black) and received (dashed black) signals of FMCW, SFCW, and OFDM radar systems. It is shown that the phase (red dots) is the same for all these.
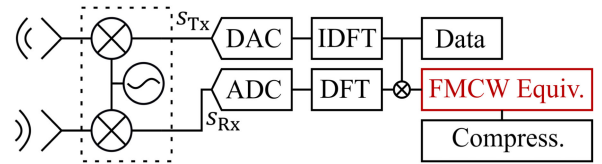

FIGURE 6. OFDM processing steps. The DFT and multiplication correlate the transmitted and received data.

TABLE 1. Constants for Different Modulation Schemes

Modulation	p
FMCW	$\dfrac{f_{\max} - f_{\min}}{T_{\mathrm{Ch}}} \cdot T_{\mathrm{S}} = \mu_{\mathrm{Ch}} \cdot T_{\mathrm{S}}$
SFCW	Δf
OFDM	$\dfrac{1}{K_{\mathrm{S}} \cdot T_{\mathrm{S}}}$

is evaluated. Therefore, the amplitudes of the raw data are dominated by a few slow, near targets at an angle of around 0°. For data processing, this indicates the presence of much redundancy that may be exploited for compression. Here, another important observation is the high range of amplitudes that needs to be preserved (at least around 40 dB for normal radars).

III. RADAR SIGNAL MODEL

In this section, we demonstrate that radar data may be interpreted as being multidimensional sinusoidal signals. With that, the motivation for using some form of frequency transformation–such as discrete cosine transform (DCT) or discrete Fourier transform (DFT)–for the compression algorithm can be explained. In this section, the common simplifications of radar processing are used [9]. This includes the independency of distance and velocity, the assumption of an effective frequency for the Doppler shift, and a plane wave or far-field assumption for angular detection. The simulations are directly based on the data model described in Section II to match the real behavior of targets.

A. MODULATION EQUALITY (DISTANCE)

Here, we will show that there is no relevant difference in a compression algorithm between FMCW, SFCW, and OFDM regarding their baseband frequency domain representation. In Fig. 5, it is shown that regardless of the transmitted and received signals, the phase of each baseband signal representation in the frequency domain is a ramp, which characterizes a beat frequency [19], [20].

Most automotive radar systems today use FMCW modulations because of their advantageous lower sampling rates and the easy removal of unwanted, direct coupling and near targets [21]. Therefore, we use this as the reference case. FMCW systems modulate their signal using a linear chirp. The beat frequency is generated by mixing the transmitted chirp with the received signal. The beat frequency of a target f_b is proportional to the distance d and the slope μ_{Ch} of the chirp.

The beat signal is sampled at an interval of T_{S}. The chirp is characterized by its slope μ_{Ch}, which is calculated by the ratio of the length T_{Ch} and the bandwidth B that is characterized by the lower $f_{\min}$ and upper $f_{\max}$ frequency limits of the chirp.

SFCW uses a continuous frequency that changes discretely after waiting for a steady state [22]. In the frequency domain, the signals behave similarly to the FMCW case as by each discrete jump, the output phase is also increased, leading to a similar beat signal with a constant beat frequency for a single target. Moreover, SFCW may be used with low sampling rates since the outputted signal does not change for one frequency step, which may be adjusted by the number of measurements needed in an amount of time. It is parameterized by its frequency step size Δf.

Other emerging technologies for automotive radar systems use signaling in the time domain. These incorporate digital modulation schemes like OFDM or phase modulated continuous wave (PMCW [23]). They are based on the (auto-) correlation of a pseudo-random sequence that can be generated by a DFT of random data or gold sequences.

The signals of this modulation scheme become similar to the beat signal of FMCW within the correlation step by applying a DFT and multiplying the result with the frequency domain representation of the transmit signal, as depicted in Fig. 6. Here, instead of transforming the signals back to the time domain, they can be used for the different compression approaches. The relevant OFDM parameters are its sample interval T_{S} and the number of samples K_{S}.

For a single target, the FMCW-equivalent phase $\varphi_{\mathrm{FMCW,E}}$ for a target n at a sample k_{S} may be represented as

$$\varphi_{\mathrm{FMCW,E}}(n, k_{\mathrm{S}}) = \frac{2\pi}{c_0} \left(2d(n) \cdot p \cdot k_{\mathrm{S}}\right) + \varphi_0(n), \quad (3)$$

with the parameter p from Table 1 for the different modulation schemes as per [9] and [14]. The factor k_{S} is in the range
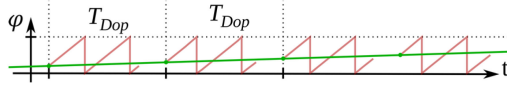
FIGURE 7. Changing of phases of signals by the Doppler effect during a longer observation period. Green shows the effects on a CW-Radar without modulation, and red shows the FMCW-equivalent modulation sequences.

$[1, K_S]$ with K_S being the number of samples. Further, c_0 is the speed of the traveling wave, $d(n)$ is the distance of target n, and φ_0 is an arbitrarily chosen start phase, which is a random constant in reality and not directly evaluated in the reconstruction.

B. VELOCITY DIMENSION (DOPPLER)

For a short time, the distance of moving targets is considered constant. A Doppler dimension is constructed by repeating similar transmitted signals over some time T_{Dop} and evaluating the changes in phase over a longer time. This is shown in Fig. 7.

With the common simplifications, this is interpreted as an additional phase term varied with the Doppler-time, which leads to an equivalent Doppler-phase $\varphi_{\text{Dop,E}}$ of

$$\varphi_{\text{Dop,E}}(n, k_D) = \frac{2\pi}{c_0} \cdot 2v(n) \cdot T_{\text{Dop}} \cdot f_{\text{mid}} \cdot k_D. \qquad (4)$$

The variable f_{mid} is hereby an equivalent center frequency used as an effective frequency since the bandwidth is usually small compared to the absolute frequency. k_D is the counting index of the sample dimension in the range $[1, K_D]$, with K_D being the number of Doppler-repetitions. Here, $v(n)$ is the radial velocity of target n.

C. ANGULAR DIMENSIONS (AZIMUTH/ELEVATION)

For angular separation of targets, an array of antennas is commonly used. The incident waves are typically simplified as planar since the distance to the target is much larger than the length of the antenna array itself. The antennas are mostly linearly spaced or at least decomposable into linearly spaced arrays since this enables easy processing by DFTs. In this context, it is irrelevant whether an antenna is used for receiving or transmitting.

In the simulation section of this paper, two orthogonal dimensions with linear arrays were used, but other variants of arrays, such as sparse arrays used in radar imaging [24], could also be used by splitting up high-order dimensional data for optimal compression. The additional phase term for the angular dimensions φ_{Ang} can be described as

$$\varphi_{\text{Ang}}(n, k_{\text{Ang}}) = \frac{2\pi}{c_0} \cdot \Delta d \cdot f_{\text{mid}} \cdot \sin\left(\alpha_{\text{Ang}}(n)\right) \cdot k_{\text{Ang}}. \quad (5)$$

Here, k_{Ang} is the counting index of the sample dimension in the range $[1, K_{\text{Ang}}]$, with K_{Ang} being the number of antenna elements in use. Δd is the spacing of the antennas. The angle $\alpha_{\text{Ang}}(n)$ is measured from the target n to the line through the antennas of the linear array, as depicted in Fig. 8.
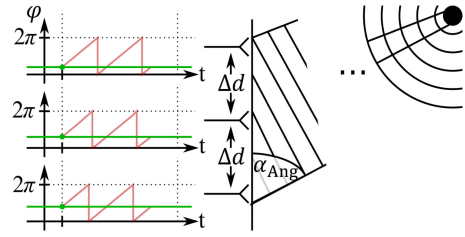

FIGURE 8. Angular detection based on linearly spaced arrays with three antennas. Green shows the change in phase for a CW-Radar, while red visualizes this for an FMCW-equivalent signal.

D. SIGNAL GENERATION

The overall phase for a given target is constructed by summing up the individual phases as

$$\varphi_{\text{Sig}}(n, k_S, k_D, k_{\text{Az}}, k_{\text{El}}) = \varphi_{\text{FMCW,E}}(n, k_S)$$
$$+ \varphi_{\text{Dop,E}}(n, k_D)$$
$$+ \varphi_{\text{Ang,Az}}(n, k_{\text{Az}})$$
$$+ \varphi_{\text{Ang,El}}(n, k_{\text{El}}). \qquad (6)$$

The signal of each target can then be constructed via trigonometric functions. The received signal is the sum of all N_{tar} individual targets. For real data, this is done by using trigonometric functions (sine or cosine) as

$$s_{\text{Sig}}(k_S, k_D, k_{\text{Az}}, k_{\text{El}})$$
$$= \sum_{n=1}^{N_{tar}} a_{\text{Path}}(n) \cdot \sin\left(\varphi_{\text{Sig}}(n, k_S, k_D, k_{\text{Az}}, k_{\text{El}})\right), \qquad (7)$$

or by using the Euler function for a complex signal as

$$s_{\text{Sig}}(k_S, k_D, k_{\text{Az}}, k_{\text{El}}) = \sum_{n=1}^{N_{tar}} a_{\text{Path}}(n) \cdot e^{j \cdot \varphi_{\text{Sig}}(n, k_S, k_D, k_{\text{Az}}, k_{\text{El}})}. \qquad (8)$$

Here, Equation (2) is used for attenuation $a_{\text{Path}}(n)$ with the angle and distance of the individual target n.

As complex data can be brought to real representation by up-sampling with a factor of two and applying an inverse Hilbert transform, the algorithms were only evaluated for real data.

This data can be ideally compressed by the usage of multi-dimensional trigonometric predictors. This can be done by a transformation to the frequency domain with a DFT or DCT and the construction of a radar cube in case of 3D data. For this reason, a DFT-based algorithm will be the simple radar signal-based benchmark for more established compression algorithms.

E. NOISE

Noise is a largely limiting factor of compression algorithms. Common radar signals can only be interpreted after applying a high correlation gain by using transformations or filtering after [25]. The final step for describing radar data is the consideration of additive white Gaussian noise (AWGN). Thus,

we use the definition of SNR without any correlation gain since the raw data are used for our investigation on compression possibilities. The final noisy, real valued data s_{Noisy} may be represented with added, zero mean AWGN noise N with variance σ^2_{Re} as

$$s_{\text{Noisy}}(k_{\text{S}}, k_{\text{D}}, k_{\text{Az}}, k_{\text{El}}) = s_{\text{Sig}}(k_{\text{S}}, k_{\text{D}}, k_{\text{Az}}, k_{\text{El}}) + N(0, \sigma^2_{\text{Re}}). \tag{9}$$

Until now, the data could have been described with little to no error by a trigonometric data model. Moreover, white noise has no correlation and can therefore not be compressed without losing information, leading to much lower compression ratios.

Consequently, the highest impact occurs in lossless data transmission since all the information needs to be transferred. However, lossy data compression suffers less since it is based on the premise of discarding the unwanted, noisy information of the signals. This is done by separating the noise and signals using some type of signal processing. In this context, multimedia codecs use the correlation gain of a DCT and remove non-perceptible signals with low amplitudes.

IV. DATA COMPRESSION METRICS

The losses introduced by lossy compression algorithms need to be quantified to ensure acceptable results. Since the further processing steps of future radar applications are not defined, we will create different metrics for a multitude of further processing steps. These metrics are tested by simply quantizing signals with different numbers of bits, as this is the most basic lossy compression algorithm.

Since the raw data is dominated by noise and therefore hardly interpretable, we use metrics based on processed range-Doppler maps [26]. We begin with metrics based on SNR followed by human perception of images. Here, the human perception metrics are seen as a reference of overall similarity. Meanwhile, the radar data itself can hardly be evaluated by humans and is therefore typically interpreted by machines; other metrics are considered for more useable use cases.

To showcase the different metrics, the simulated scene with the range-Doppler map in Fig. 9 is displayed. The original data were sampled at 16 bits. An SNR of 0 dB between the simulated signals and the defined signal was used to add realistic noise. This data is then uniformly quantized to a different number of bits. For each metric and each resulting bitrate of our basic reference quantization algorithm, we performed 50 repetitions to obtain statistically interpretable results for different simulated scenes.

A. SNR-BASED METRIC

The first metric uses the SNR, which is a standard metric for depicting the similarity of two signals. The metric was calculated using the original, uncompressed raw data of the
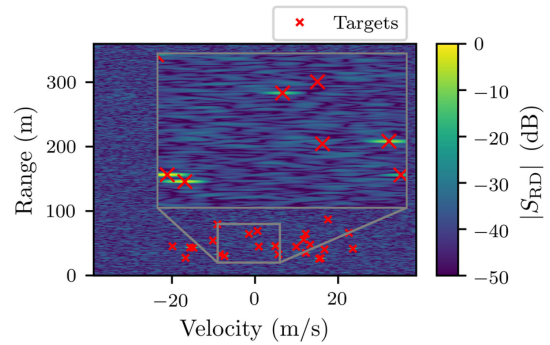

FIGURE 9. Range Doppler processed raw data (16 bit) for displaying and evaluating the proposed metrics. The red crosses show the 25 simulated targets with their corresponding distance and velocity transformed to the radar coordinate system. The received power is corrected with the radar equation from (2). Therefore, not all of the targets are visible above the noise floor. For the metrics, only the highlighted section is displayed since the influence is more visible by zooming in instead of showing the whole range-Doppler map.
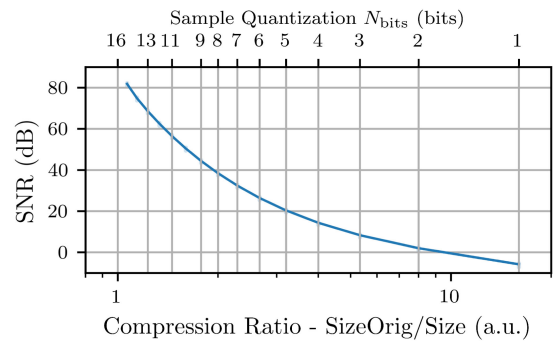

FIGURE 10. SNR values for different quantization stages (1 to 16 bit). The SNR is similar for each run; therefore, the error margins are not visible unlike in the other metrics.

ADC and the decompressed equivalent with

$$SNR = 10 \cdot \log_{10} \left(\frac{\text{E}(X^2_{\text{Orig}})}{\text{E}\left(\left(X_{\text{Orig}} - X_{\text{Comp}}\right)^2\right)} \right). \tag{10}$$

The operator E is the expected value of the data arrays. The original data array, which is denoted as X_{Orig} and X_{Comp}, represents the decompressed array that is used. All samples of each dimension are treated equally in this case.

For quantization, this metric has simple results, since the values are only quantization errors, which is similar for all repetitions. It can be calculated with a formula similar to the quantization error of a uniformly distributed full range signal [27] as

$$SNR(N_{\text{bit}}) = (K + 6.02 \cdot N_{\text{bits}})\text{dB}$$

$$\approx (-11.94 + 6.02 \cdot N_{\text{bits}})\text{dB}. \tag{11}$$

Here, the sample quantization characterized by its number of bits N_{bit}. Meanwhile, the offset K is determined by experiment. The results of this metric are depicted in Fig. 10.
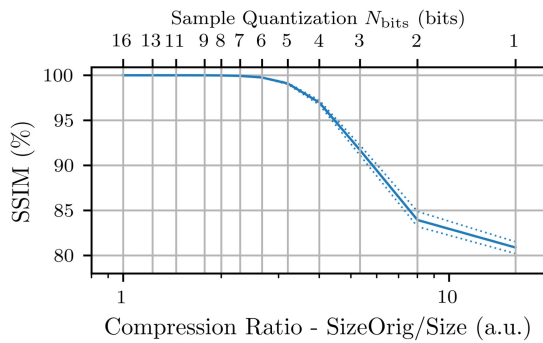
FIGURE 11. SSIM values for different quantization stages (1 to 16 bit). The error bars and dotted lines characterize the first and third quantiles of 50 runs.
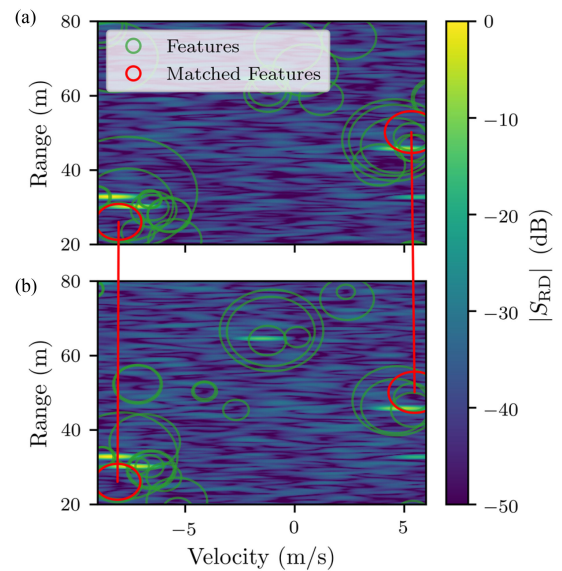

FIGURE 12. SURF features for the range-Doppler map. Highlighted in red are the features that are similar in the original image in (a) and the 3-bit compressed image in (b).
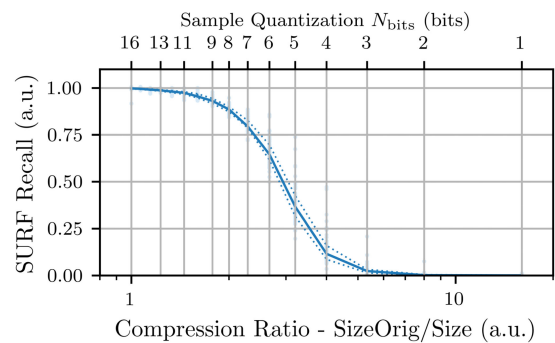

FIGURE 13. SURF features for the range Doppler map for different quantizations (1 to 16 bits). The error bars and dotted lines characterize the first and third quantiles of 50 runs.

B. HUMAN PERCEPTION-BASED METRIC

The second metric is based on the structural similarity index measure (SSIM) [28]. This algorithm compares a reference image x with a changed image y and computes a difference image. The formula may be described as

$$SSIM(x, y) = \frac{(2\mu_x\mu_y + c_1)(2\sigma_{xy} + c_2)}{(\mu_x^2 + \mu_y^2 + c_1)(\sigma_x^2 + \sigma_y^2 + c_2)}. \quad (12)$$

The variables μ_x, μ_y represent the average and σ_x, σ_y the variance of x and y, respectively. The term σ_{xy} is the covariance of the images. The constants c_1, c_2 stabilize the division. Equation (12) was performed on the logarithmic range-Doppler maps, as displayed in Fig. 9. Moreover, logarithmic scaling was used since the linear scaled power can easily span multiple decades (see Fig. 9). In the linear scale, there is hardly any distinction between noise that is at -50 dB equaling 10^{-5} and the targets with low levels at -20 dB equaling 10^{-2}. In the following quantization step, this did not have any impact compared to the targets with the highest power of 0 dB equaling 1. The quantization was chosen as 8 bits for a standardized gray scale.

The measurement was repeated for all different quantization steps and 50 times for different scenes. The error bars characterize the first and third quartiles of the values. The same cropped number of bits were grouped and the error bars were calculated, forming the graph in Fig. 11.

The above metric is an indication of how well the overall representation changes. Here, small changes did not change the index largely. By optical inspection, values below 85% are proof of insufficient alternations in the results. These indicate losses of small targets, and the overall optical representation decreases. For all quantized values above 3 bits, this holds. Therefore, this metric should not be used for applications where small changes are important.

C. MACHINE LEARNING FEATURE-BASED METRIC

Machine learning uses feature extraction on images for detection of similar regions in other images. The "Speeded Up Robust Features" (SURF) [29] is widely used for these tasks. This algorithm searches for visually interesting features in an image and generates a feature vector based on the internal statistics. By comparing the features of two different images, similar regions can be found. Features for the original and the image represented by 3 bits are highlighted in Fig. 12.

The total number of matched features in comparison to all features was used as the SURF-recall metrics value. This was again repeated 50 times and is depicted in Fig. 13.

This metric is a representation of how well optical features are preserved. Hereby, the settings are the overall number of features found in the image and the certainty of a matched target. Further, these were chosen rather strictly to achieve an overview whether the data can be used "as is" after decompression.

In this figure, low values of this metric (<0.1) indicate that there are only few matching features, leading to the requirement for lower boundaries to match those features, thereby increasing the chances of mismatches. This might lead to the
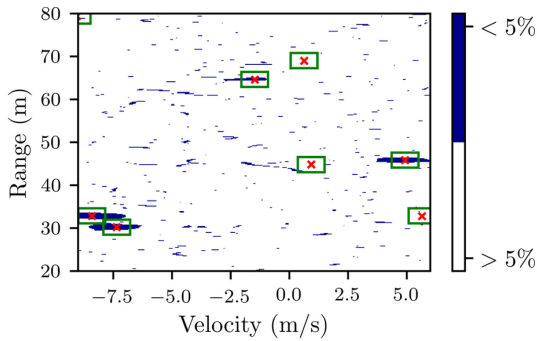
FIGURE 14. Areas that have an error that is higher than 5% at the 3-bit quantization. The green boxes mark the spaces around point targets, which are considered in this metric.

FIGURE 15. Percentage of the area around the targets that have an error smaller than 5% for different quantizations (1 to 16 bit). The error bars and dotted lines characterize the first and third quantiles of 50 runs.

need to retrain the algorithm. Moreover, this metric represents the losses well, but focuses more on the noisy parts than the real data. As depicted in Fig. 12, the features are located both in noisy regions and in parts with targets.

D. RANGE DOPPLER ERROR-BASED METRIC

While visual-based data processing needs to be conducted on data that is real-valued and scaled logarithmically, the next metric works on the range-Doppler-processed data directly. This has the advantage of detecting phase mismatches that would be removed otherwise. This metric was chosen so that only a small area (of 20×20 pixels) is used around each point target (shown in Fig. 14) that needs to be preserved. For each pixel within this area of interest, a relative error x_{Err} is calculated by

$$x_{\text{Err}}(r, d) = \frac{\left|x_{\text{Orig}}(r, d) - x_{\text{Comp}}(r, d)\right|}{0.5 \cdot \left(\left|x_{\text{Orig}}(r, d)\right| + \left|x_{\text{Comp}}(r, d)\right|\right)} \cdot 100\%,$$

(13)

to take the high dynamic range of several decades into account. The values x_{Orig} and x_{Comp} are hereby the complex numbers representing each individual pixel at range index r and Doppler index d in the range-Doppler plane.

For each of the calculated values, we then evaluated whether the error is lower than 5%. This metric's value was then calculated by the ratio of "good" cells to all cells that are tested, and the results are displayed in Fig. 15.

There is no human perceivable loss in targets at above 50% in metric value since a relative error of 5% is not visible at all by visual inspection. Further, if 50% or less pixels in the image have this low error value, this is not perceivable at and around the targets. Thus, every value above 10% is considered a good representation of the targets. This means that even in the 1-bit case, the targets are represented good to a certain degree. Furthermore, because of the conversion gain, the point targets are good represented at their highest point, as seen in Fig. 14. This figure represents a metric value of around 25%. There are some targets with an error above 5%, but many targets are represented within this margin of error. Since this metric is formed on the targets, it is more useful for radar data.
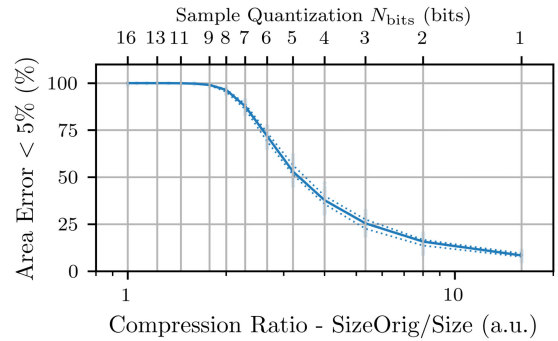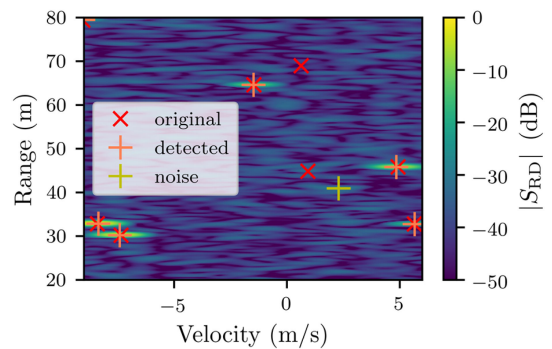

FIGURE 16. CFAR detections for the uncompressed 16-bit original data. The red crosses show the original simulated point targets. The orange crosses show correctly detected targets. The yellow are false alarms generated by noise.
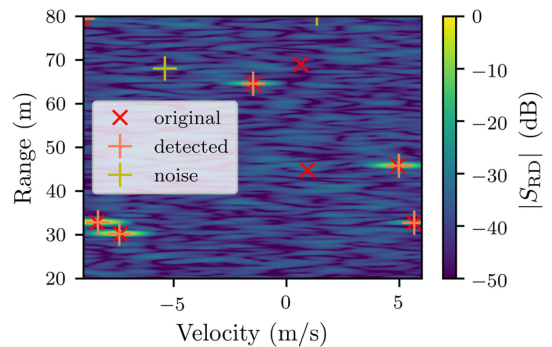

FIGURE 17. CFAR detections for the processed data with 3-bit quantization. The red crosses show the original simulated point targets. The orange crosses show correct detections. The yellow are false alarms generated by noise.

E. CFAR FEATURES BASED METRIC

Modern radar systems use constant false alarm rate (CFAR) algorithms [30], which estimate the noise in a certain area, to extract point targets from radar cubes. Here, if a central point is above this noise estimate by some margin, it is interpreted as a valid target. However, upon comparing Fig. 16 with Fig. 17, it is not easy to distinguish between targets that need to be kept
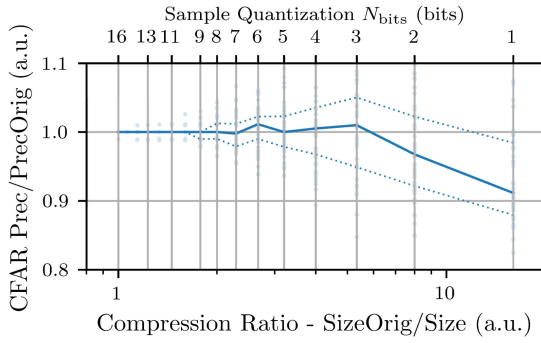
FIGURE 18. Change in precision of the quantized data (1 to 16 bit) in comparison with the original data. The ratio can be higher than one because the actual precision can be larger than the original because of fewer false detections. The error bars and dotted lines characterize the first and third quantiles of 50 runs.
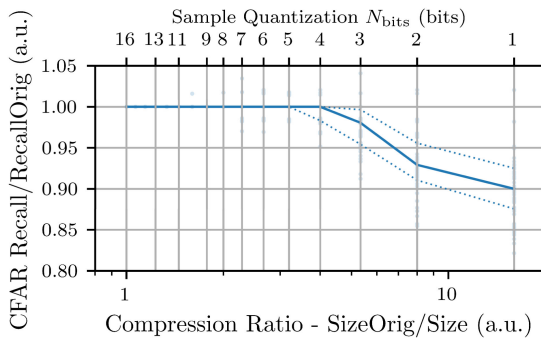

FIGURE 19. Change in recall of the quantized data (1 to 16 bit) in comparison with the original data.

and those that do not. Here, we attempted to match the CFAR point targets with the underlying simulation targets. In this way, we were able to generate a more robust metric since it removed the CFAR uncertainty. The metric is processed using the following steps:

- Process the targets detected with CFAR from the original radar data for recall and precision
- Process the decompressed radar data again for recall and precision
- Compare both results by determining a ratio between the actual and original precision to remove the influence of the CFAR algorithm itself

In Fig. 16, the original 16-bit data with its CFAR results are displayed. Meanwhile, the 3-bit quantized and processed data in Fig. 17 shows that the noise level is slightly increased and the noisy targets are different. The real targets were mostly detected correctly in this scenario. This metric was then repeated 50 times for all variants, and the results are displayed in Fig. 18 and 19.

For the proposed metric, the optimum value is 1.0, leading to exactly the same CFAR results as before. Values above 1.0 indicate fewer targets based on noise or more correctly detected targets. This can occur if a target was originally surrounded and shadowed by noise. Moreover, quantization to a lower number of bits can slightly decrease the noise in its
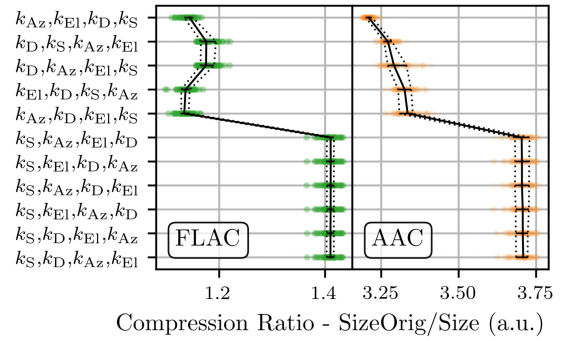

FIGURE 20. File sizes for AAC and FLAC with selected permutations of the data array. The error bars and dotted lines characterize the first and third quantiles of 50 runs.

surroundings so that the target becomes visible. This could be interpreted as denoising by quantization that occurs in other signal processing as well. The opposite can occur in the case of wrong noise detections. Thus, for this metric, the values were chosen more strictly than before since this would largely impact the perception of targets. More specifically, precision and recall values below 0.8 were considered insufficient, indicating a loss of 20% of the targets or an addition of 20% of wrongfully detected noise targets.

V. DATA COMPRESSION ALGORITHMS

Data compression is done with the goal of removing redundancy and unneeded data. For the simulation, we used four-dimensional (4D) input data, which are the sample or distance dimension (k_S), the velocity dimension (k_D), and the two angular dimensions for azimuth (k_{Az}) and elevation (k_{El}). In a first step, it was necessary to identify the dimensions with the largest redundancy. For this, we used the free lossless audio codec (FLAC) as a lossless and the advanced audio codec (AAC) as a lossy compression algorithm, which will later be discussed more comprehensively. These algorithms were configured to use a single channel, and different permutations of the 4D data are shown in Fig. 20.

An example for this permutation process can be done by simplifying to a two dimensional array with the indexes k_D and k_S. This array can be permuted in two ways k_D, k_S and k_S, k_D. The permutation to a one-dimensional (1D) array with length of $K_D \cdot K_S$ can be done with

$$s(k_D, k_S) \rightarrow [s(0, 0), s(1, 0), \cdots, s(K_D, 0),$$
$$s(0, 1), s(1, 1), \cdots, s(K_D, 1),$$
$$s(0, K_S), \cdots, s(K_D, K_S)] \quad (14)$$

for the first permutation, and

$$s(k_S, k_D) \rightarrow [s(0, 0), s(1, 0), \cdots, s(K_S, 0),$$
$$s(0, 1), s(1, 1), \cdots, s(K_S, 1),$$
$$s(0, K_D), \cdots, s(K_S, K_D)] \quad (15)$$

for the second permutation.

According to the results shown in Fig. 20, the most influential dimension is k_S because of the high number of samples and the steep decline in the amplitudes of signals with higher frequencies (compare equation (2) and Fig. 4). The order of the remaining dimensions does not show a high influence. From here on, the best permutation $[k_S, k_D, k_{Az}, k_{El}]$ from the results in Fig. 19 is used for all further compression algorithms.

The following sections show a variety of different multimedia compression algorithms that we use to compress the data. We compare these algorithms to a proposed DFT-based algorithm that utilizes the established radar signal properties of Section III nearly ideal.

A. LOSSLESS COMPRESSION ALGORITHM
Lossless compression algorithms remove redundancy and use entropy coding on the resulting data [31]. Since all information is preserved, the benefits are rather limited because of the low SNR of the original data, this includes transformations of the data, which can also be seen in Fig. 25.

However, with these, it is possible to gain a compression ratio of around 1.4 which corresponds to 70% of the original full scale range used by the ADCs. Therefore, we only incorporated results for the FLAC, which is an audio algorithm from the FFmpeg collection [32] in this paper. Meanwhile, other lossless compression algorithms could not improve these results significantly since the noise, which has high, uncorrelated, and therefore uncompressible information, needs to be preserved.

B. AUDIO COMPRESSION ALGORITHM
Audio data is arranged as 1D data for each channel with only a limited number of channels. This means that for audio compression, the index k_S is used for time signaling, and the other channels are ordered sequentially. Therefore, audio compression is mostly 1D, but there may be additional channel decorrelation steps for multichannel optimized algorithms. Here, we deployed the AAC [33] and the free Ogg Opus [34] codec from the FFmpeg collection [32]. Both show the tendency to remove high frequency components as well as apply some kind of noise shaping, as shown in Fig. 21.

The compression ratio does not benefit largely from using multiple channels since the algorithms are solely based on simple decorrelation attempts of channels. The sample rate was chosen to be relatively low at 24 kHz to obtain all frequencies in the audible frequency range. The compression parameters for audio compression algorithms are selected in relation to this since they characterize a target data rate.

C. HEVC VIDEO COMPRESSION ALGORITHM
For video data compression, the input data were arranged in consecutive images. In each image, the horizontal position corresponded to the sample index k_S, the vertical position to the chirp index k_D, and the azimuth and elevation index were multiplexed to the time index of the video. The resulting sequence was then encoded with the HM-16.22 [35] encoder
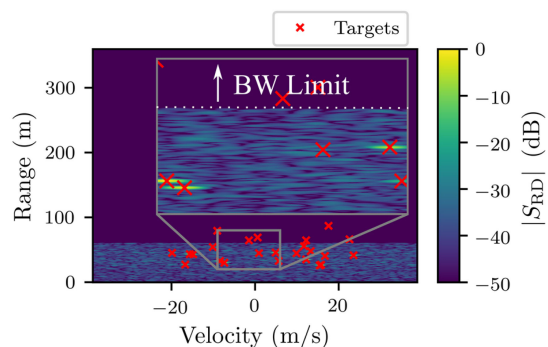

FIGURE 21. AAC compression using psychoacoustic processing characterized by a bandwidth limit. A bit rate of 10 kBit/s was chosen for this scene for visualization purposes of the effects of AAC. In reality, this would lose some targets, and therefore, a higher bitrate is probably necessary.
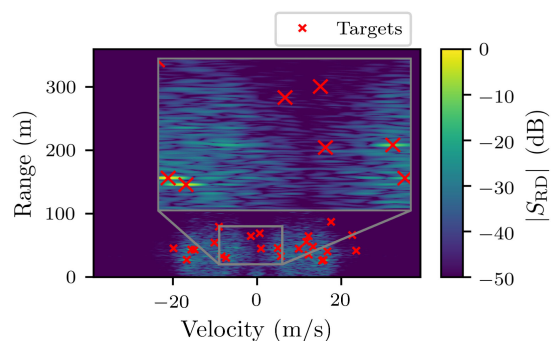

FIGURE 22. HEVC compression of the simulated scene. The HEVC quantization setting QP was set to 46. Here, it is clearly visible that HEVC has some regions of interest, which are conserved. In reality, this would lose some targets, and therefore, a higher bitrate is probably necessary.

implementation of the high-efficiency video coding (HEVC) codec [36]. The encoder was configured with the random-access encoding configuration [37] at a bit-depth of 16 bit per sample in the 4:0:0 color format, which means that the sample value is coded as a single color component (which is equivalent to the luminance). The results for this compression algorithm are displayed in Fig. 22. Here, the value 46 was chosen as quantization parameter (QP) to visualize the compression artifacts.

In comparison with audio compression, video compression provides several advantages when compressing radar signals. First, video compression exploits three dimensions for redundancy reduction (two spatial and one temporal dimension), whereas audio usually only exploits one dimension. Second, the block-based partitioning scheme allows for an efficient representation of large areas of the radar-based images. Finally, sophisticated prediction tools–such as motion compensation, in which the content of a previously coded image is used to predict the content of the current image–can exploit similar content in different images to increase compression performance.

D. SIMPLE DFT-BASED COMPRESSION ALGORITHM

All algorithms previously described are based on multimedia codecs. For comparison purposes, a real-valued DFT-based algorithm was used for comparison. This is based on the assumption that with the correlation gain from the DFT, separation/extraction of features is possible. Low values can be removed by setting these values to zero when they fall under a threshold for an estimated noise floor. Here, another advantage lies in the quantization stage, which can be scaled logarithmically which is more suitable for radar-based processing. Moreover, radar signals have a high dynamic range (cf. Fig. 4), and for that, the linear representation is too precise for high values. However, the downside of this approach is its non-standardized processing chain, which is not readily available in hardware. The encoder based on the DFT consists of the following five steps:

- Transformation via n-dimensional real-valued DFT by discarding negative frequencies
- Switching to a representation with phase and logarithmic amplitudes
- Removal of the noise floor by setting values below a predefined amplitude threshold to zero
- Quantization of the resulting values
- Lossless entropy coding with a Lempel-Ziv-Markov-algorithm (LZMA) [38] for showcasing purposes

The decoder follows these steps in the reverse order.

In the first step, the DFT decorrelates the real valued data, which can be considered a pulse compression for the data defined in (9). It is transformed to the frequency domain and can separate amplitude and phase information in the next step. The phase information is nearly uniformly distributed [39] (cf. Fig. 25) and may not help separate targets from noise. Therefore, the phase information is not considered for the first theoretical part. The DFT is a linear transform, meaning the sum in s_{Noisy} (9) can be transformed separately.

The amplitude of one target n can be written after transformation [40], [41] as

$$\left| S_{Sig}(\vec{l}, n) \right| = \frac{K_S K_D K_{Az} K_{El} a_{\text{Path}}(n)}{2} \left| \text{sinc}(\vec{l} - \vec{l}_n) \right|, \quad (16)$$

with $\vec{l} = [l_S, l_D, l_{Az}, l_{El}]$ being the vector of the transformed data coefficients $[k_S, k_D, k_{Az}, k_{El}]$. The running indices of the DFT as $l \in [0, K/2]$. $\vec{l}_n$ represents the position of the target in the DFT coordinates, which could also be fractional numbers. This allows a simpler, arbitrary description since the compression is not dependent on the real world axis scaling. Further, the conversion factors can be obtained through the defining formulas (3) to (5). The multidimensional sinc $\text{sinc}(\vec{l})$ is defined as per [40] as

$$\text{sinc}(\vec{l}) = \prod_{m=0}^{M} \frac{\sin(\pi l_m)}{\pi l_m}, \quad (17)$$

with $\vec{l}$ being a vector of length M representing the different dimensions (e.g., distance, Doppler, azimuth, elevation).
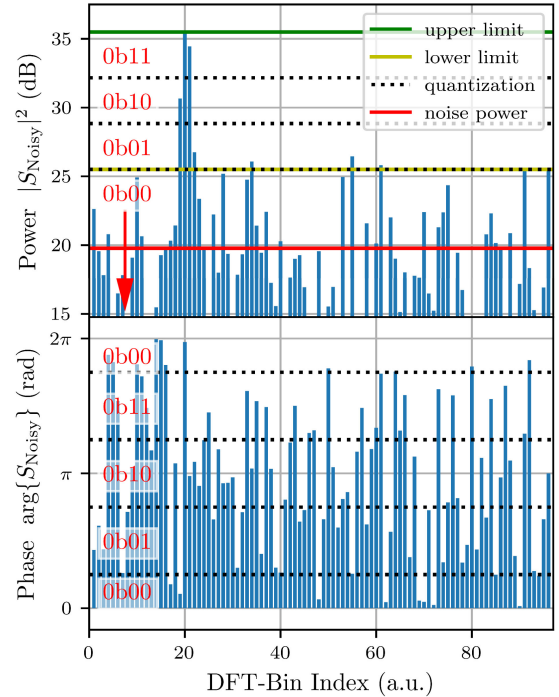

FIGURE 23. Signal power and phase of a real-valued DFT of a sine with AWGN. This sine is shown in the two bin indexes around 20. The yellow line characterizes the lower quantization limit; everything below this limit is removed. The black lines show the quantization stages for 2 bits. Since the phase is noisy, most of the information is concentrated here.
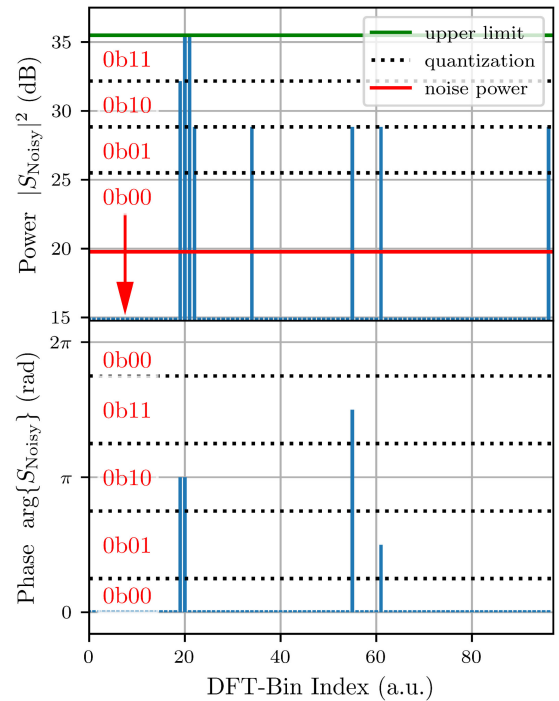

FIGURE 24. Spectrum after quantization and decimation of data. The values for the de-quantization above zero are chosen to be the maxima. In the amplitude case, different values are effectively an attenuation or amplification. The values for the zero case could be chosen arbitrarily since they will not transfer any information. The phase value are set to zero at the lowest amplitude values, since they have no influence.
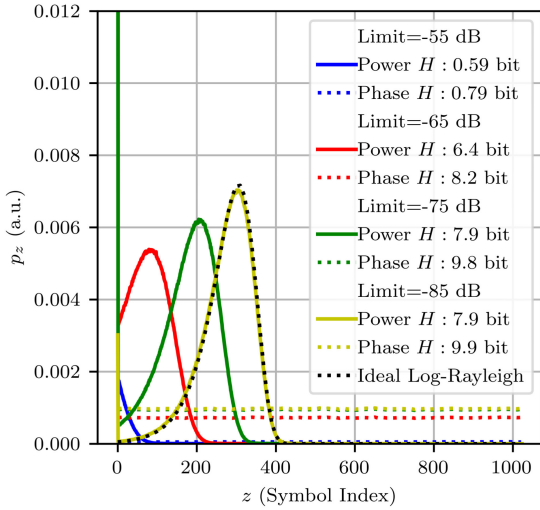
FIGURE 25. Histograms (PDF) of 10-bit quantized data with different limits from −55 dB to −85 dB. The bin 0 is not shown in full, since this single bin becomes too large to overshadow any effects in the other bins. The power values of the noisy parts are visible as a defined peak. The phase values are evenly distributed. With lower limits for cutoff, more of the noisy parts are removed. The entropy H decreases accordingly. The ideal log-Rayleigh-distribution shows that most of the signal corresponds to the established noise distribution.

With the assumption of independent AWGN with zero mean, the noise can also be transformed to the frequency domain as per [39] as

$$S_{\mathrm{Noise}}(\vec{l}) = N_{\mathbb{C}}\left(0, \frac{K_S K_D K_{\mathrm{Az}} K_{\mathrm{El}}}{2}\sigma_{\mathrm{Re}}^2\right). \qquad (18)$$

The transformation generates complex zero mean white noise $N_{\mathbb{C}}(0, \sigma_{\mathbb{C}}^2) = N(0, \sigma_{\mathbb{C}}^2/2) + 1\mathrm{j} \cdot N(0, \sigma_{\mathbb{C}}^2/2)$ with two independent white noise processes with scaled variance $\sigma_{\mathbb{C}}^2/2$ and the power of the original signal. This is also intuitive since the power needs to be constant and is transferred to both the real and the imaginary parts equally. The two real valued bins of a DFT at 0 and $K/2$ are different, with $S_{Noise}(\vec{0}) = N(0, K_S K_D K_{\mathrm{Az}} K_{\mathrm{El}} \sigma_{\mathrm{Re}}^2/2)$. For the following examinations this is neglected, since those are only two bins in the whole N-dimensional DFT. For this process, the amplitude $|S_n(\vec{l})|$ becomes Rayleigh distributed and the logarithmized values become Log-Rayleigh distributed [39], [42]. This distribution is observed in Fig. 25.

The variable S_{Noisy} is the sum of the signal and noise part. The SNR after the correlation gain SNR_{COR} is then derived from (16) and (18). For this, the optimal values are assumed, by definition, as the sinc is evaluated at its maximum with $|\mathrm{sinc}(\vec{l} - \vec{l}_n)| = 1$ and $a_{\mathrm{Path}}(n) = a_{\max}$. Here, the attenuation is also at its maximum. By applying the common radar-SNR equation of a single bin, it can be written as

$$
\begin{aligned}
SNR_{\mathrm{COR}} &= \frac{P_{\mathrm{Sig}}}{P_{\mathrm{Noise}}} = \frac{|S_{\mathrm{Sig}}|^2}{|S_{\mathrm{Noise}}|^2} \\
&= \frac{K_S K_D K_{\mathrm{Az}} K_{\mathrm{El}}}{2} \cdot \frac{a_{\max}^2(n)}{\sigma_{\mathrm{Re}}^2}.
\end{aligned} \qquad (19)
$$

The gap between signal and noise becomes larger upon the increasing of the number of samples. Further, removing the noise floor removes most of the data, causing most of the information to also be taken away with the corresponding phases. Subsequently, the resulting data is quantized.

A 1D case of a single target is visualized in Fig. 23. Here, the DFT of length 192 transformed a sine of amplitude 1.0 with additive white noise and an SNR of 0 dB. Theoretically, this would yield a power level of 39 dB by formula (16) after transformation. However, the sinc is not at its maximum peak, leading to around half (33 dB) of the power. In combination with the noise power, the maximum amplitude is 35 dB. The conversion gain, and consequently, SNR_{COR}, can be characterized by the difference of the noise power to the upper limit. Because of the multiplicative nature of the multidimensional $\mathrm{sinc}(\vec{l})$ [40], the potential of noise removal for N-dimensional data is even higher. The quantized and decimated data are shown in Fig. 24. Here, it is visible that most of the noisy parts are removed.

Assessing these results can be done by calculating the entropy. The entropy characterizes the mean information of each sample in bits and can be defined as a measure of the amount of possible compression by entropy coding. The entropy H in bits is defined as per [43] as

$$H = -\sum_{z=0}^{Z} p_z \cdot \log_2(p_z), \qquad (20)$$

with p_z being the probability of a symbol z that is a representation of the quantized data. The probability of each symbol can be assessed by a histogram of many samples of data.

To showcase this data, the normed histograms are shown in Fig. 25 for different limits (−55 dB to −85 dB) and 10-bit quantization. These normed histograms can be interpreted as the estimates for a probability density function (PDF), which is then used for the entropy analysis of the simulated data. The x-axis of Fig. 25 shows the Symbol index for the 1024 10-bit values, and the y-axis shows the probability of this symbol.

For the highest limits (−85 dB), the most values (Index 100 to 400), by far, correspond to unneeded, noisy parts. This can be concluded, since this follows nearly a log-Rayleigh distribution that is expected from transformed and logarithmized noise. Here, detectable targets are by definition above the noise (400 to 1024), but are too unlikely to have an impact on the PDF. However, by increasing the limit (−75 dB), the "noise-peak" was shifted to the left, and the lower noise amplitudes were clipped to the bin 0. Nevertheless, this clipped data is not enough to make a visible change to the phase distribution. By increasing the limit even further (−65 dB), even more of the noisy data is transferred into the zeroth bin. This many data in the bin 0 has effects on the uniform distribution of the phase. When removing most of the noisy data (−55 dB), the most data, by far, for the phase as well as the amplitude are in the zeroth bin, which corresponds to a low entropy. Moreover, the overall height of the peak decreased for higher limits because of the narrower
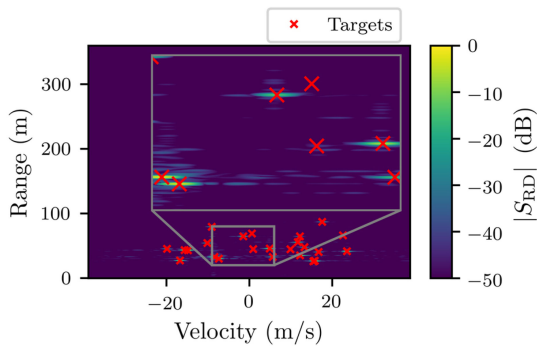
FIGURE 26. DFT-based compression. In this case, the DFT is limited to −55 dB. The data were quantized with 3 bits for both amplitude and phase.

FIGURE 27. Comparison of the different compression algorithms using the SNR metric (lower means better). The tendency of all algorithms is the same, with HEVC as the best, Audio as the second, and DFT as the last.

quantization stages (See Fig. 23). The combined entropy of the power and phase is the mean of the singular values since both needed to be transferred. Here, the 10-bit quantization case lead to 0.69 bits, while 3-bit quantization of the same simulated data can reach an entropy of 0.0092 bits.

Entropy is the theoretically best value for uncorrelated data. However, even the transformed data has some redundancy, which is exploited by the LZMA algorithm that is later applied. The redundancy is, for example, the comparable values of each sinc function. With this, the LZMA algorithm achieved data compression by an additional factor of around two to three compared with the entropy.

The investigation of the minimum quantization of the logarithmic data is done later. However, the results showed that 2 bits for the amplitude is not enough. Quantization above 3 bits showed sufficient results, with higher levels becoming more precise. The phase did improve steadily to around 8 bits. Above that, not many improvements have been observed. In Fig. 26, the results of this compression algorithm are shown. Here, the noise floor was cut at a value of −55 dB of the highest value. With that setting, the noise was nearly completely removed but left many of the lowest targets.

As seen, the limit set for noise floor removal has the highest impact on the compression ratio. In the simulation results section, this varied from −30 dB to −90 dB of the highest value. Further, the quantization for the result done on the logarithmic amplitude and phase showed better results compared to the linear Amplitude and phase as well as imaginary and real numbers.

VI. SIMULATION RESULTS

For this simulation, different random seeded scenarios were constructed to test different compression algorithms. The established metrics were used for analyzing the results. For each scene, 100 point-targets were simulated with arbitrary chosen parameters. The simulated ADC samples were chosen to ideally use the full scale of the 16-bit data. For all algorithms with all settings, 50 different sceneries were simulated. The 25 and 75 percentiles were constructed from these and displayed as error bars.
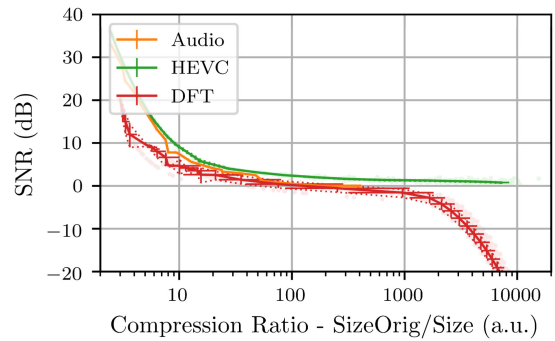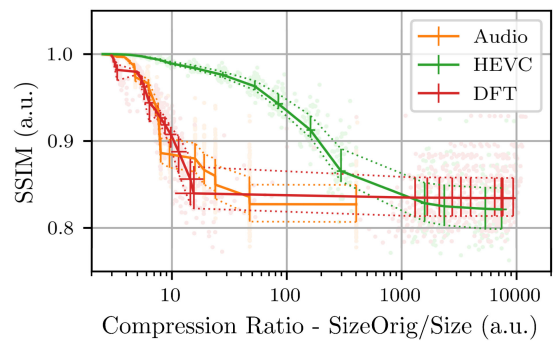

FIGURE 28. Comparison of the different compression algorithms using the SSIM metric of the processed data. The audio- and DFT-algorithms behave similarly because both are not based on visual reproduction as opposed to the video-codec HEVC.
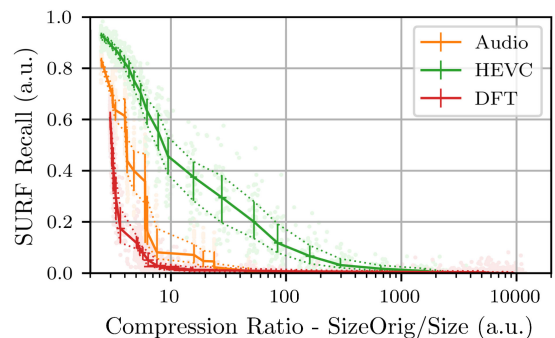

FIGURE 29. Comparison of the different compression algorithms by using the SURF recall metric of the processed data. Here, the audio- and DFT-algorithms again behave similarly, because the metric is also a visual comparison for which the video-codec HEVC is designed.

The compression parameters of the different algorithms were chosen in a wide variety of values. In Fig. 27 to 32, the plots only show the Pareto optimal parameters for each compression algorithm. This means that no better value exists at least in one value (either metric value or compression ratio). Moreover, the audio codecs were shown to work similarly and are combined for better readability. However, the FLAC algorithm is not considered here because it produces perfect
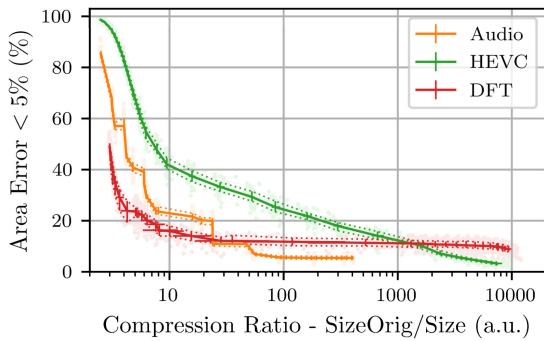
FIGURE 30. Comparison of the different compression algorithms by using the "Area Error" metric. For lower compressions, the HEVC algorithm shows the best results. The DFT algorithm does not perform well for low compression rates, but does not decrease as significantly as the HEVC. The useful audio algorithm compression ratio is rather limited.
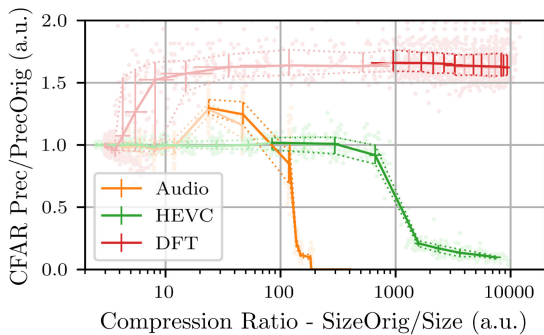

FIGURE 32. Comparison of the different compression algorithms by using the CFAR recall metric. Results above 1 indicate that targets in the original were shadowed by noise, which was removed due to compression. Here, the DFT algorithm again produces the best results. HEVC also provides reasonably good results. Only the audio algorithms suffer from limited compression ratios.

FIGURE 31. Comparison of the different compression algorithms by using the CFAR precision metric. Results above 1 indicate that there are fewer targets caused by noise than in the original image. Non-Pareto optimal results have been included as grayed out to show a trend in the codecs, since the metric is not strictly increasing because of its design.

results, which are limited to a compression ratio of only around 1.4 (cf. Fig. 20) The first metric is the SNR metric; the results are depicted in Fig. 27. This metric shows similar behavior for all compression algorithms, with HEVC being the overall best with a smooth decreasing SNR. The audio compression results are were within 5 dB of the HEVC results. The DFT performed the worst at 10 to 15 dB below HEVC. Above 1000, the DFT decreased rapidly to over 20 dB.

The second metric in Fig. 28 is based on the SSIM metric. As established before, values below 0.85 indicate large differences in the image representation of the data. If a visual representation is desired, the HEVC algorithms preserve most data until a compression ratio of around 200. Because of noise removal and bandwidth limits, both the audio and the DFT-based algorithm exhibit no satisfactory results for this metric. Their results are only usable up to a compression ratio of 10.

The next metric shown in Fig. 29 is the SURF-Features recall metric. Values below 0.1 were considered useless for direct interpretation. The HEVC again profited from its focus on image data. The recall was good for compression ratios
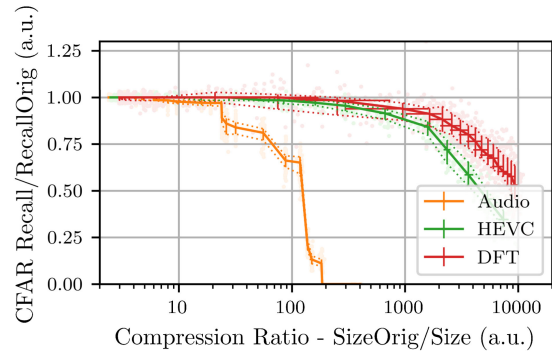
above around 100 and steadily increased. The audio and DFT algorithms again decreased fast, and usable compression ratios ranged up to about 5.

The "error of area" metric (cf. Fig. 30) is the first metric designed for the radar-data use case to preserve required data since it distinguishes between wanted targets and noisy regions. The audio compression algorithms were usable up to compression ratios of 20. The HEVC decreased steadily and was useful to around 1000. The DFT algorithm initially decreased fast because of the logarithmic scale and low quantization but did not fall below 10% until a compression ratio of about 10000.

The radar-based CFAR metrics shown in Fig. 31 and 32 are used as the final benchmark. The audio algorithms cut off high frequencies for lower compression ratios, and at about 20, the noise and the lost targets vastly increased. The HEVC algorithm did not decrease the noise largely near targets, as can be seen in Fig. 21. Therefore, there is no clear overshoot of this algorithm in the precision metric. The number of targets decreased at compression ratios of around 1200. The DFT showed a large overshoot since nearly the entire noise was removed, which increased the precision of the CFAR largely compared to the original data. However, the DFT algorithm began to lose a significant number of targets at compression ratios below 2500.

The SNR metric and image-based metrics (SSIM and SURF) favored the HEVC video codecs. The DFT-based algorithm showed its strength when radar-based metrics (Error of Area and CFAR) were considered. It becomes obvious that the high-dimensional radar data is not suitably compressed using audio compression, which incorporates a maximum of two dimensions for processing.

As a last benchmark, the processing power used in this setup was examined. The simulation was performed using a single CPU core on the same processor for all algorithms. The HEVC algorithm took the longest time, with about 3 minutes for compressing the data. The DFT compression required

TABLE 2. Constants for Different Modulation Schemes

Variable	Parameter	Description
T_S	18.7 ns	Sample interval
K_S	4096	Number of time samples
T_{Ch}	76.8 µs	Chirp duration
f_{min}	77 GHz	Lower frequency
f_{max}	78 GHz	Upper frequency
T_{Dop}	241.9 µs	Doppler interval
K_D	336	Number of Doppler Samples
Δd_{Az}	2 mm	Antenna spacing in azimuth dir.
K_{Az}	48	Number of virtual antennas

FIGURE 33. Measurement scenery with a moving pedestrian. The radar faces several obstacles such as a lamppost and a container. The path of the pedestrian is outlined by a white arrow.

around 1 minute, which was reduced to about 30 seconds for the audio signal. These results are not suited as absolute measures and were only set in relation on the same machine with a single thread. Further, results based on parallelization or other improvements like hardware acceleration for highly optimized real-world applications may vary significantly.

VII. EXPERIMENTAL VERIFICATION

To assess the possibilities of the proposed compression algorithms, we conducted several radar measurements (cf. Fig. 30) with the state-of-the-art AVR-QDM-110 12TX-16RX-MIMO radar system [44] from Analog Devices, which is based on their 77-GHz CMOS integrated radar chip called "DigiM-MIC." Here, the multiplexing scheme for TX antennas is realized using time division multiplexing (TDM). To increase the maximum unambiguous velocity range to ±4m/s, we only used three of the 12 available transmit antennas. On the receiving side, we used all 16 receive antennas, as the number of data channels does not affect the unambiguous velocity. Moreover, the radar uses FMCW modulation schemes and outputs both processed radar cubes and "raw" ADC data via Ethernet. The latter enables application-specific processing, including our compression analysis. Further, the system can be configured with a wide variety of parameters, including ramp slope, number of receive and transmit channels, or sample rate.

We chose the parameters displayed in Table 2, which are suitable for automotive radar applications in urban surroundings with pedestrian detection in mind. The parameters are extensively explained in Section II.

For the real data, no metrics are used because it is not possible to generate a trustworthy radar metric without knowing the exact ground truth of the data.

- The SNR metric is highly misleading since radar data already has a low SNR. The noisy portion results are kept in a good SNR but may not have kept the interesting parts comparable.
- Since radar data has a high dynamic range, algorithms like SSIM or SURF underestimate the importance of

visually not interesting data, which are visually not consistent above the noise. This was the case for the pedestrian in Fig. 29.
- The "Error of Area" metric needs to have information on an area of interest. However, the question of "which area should be kept" is a highly opinion-based and therefore subjective decision.
- The CFAR algorithm loses or produces targets based on noise and its settings. However, tuning the settings for high sensitivity would lead to many features based on noise that do not need to be kept. Further, tuning the parameters for low sensitivity would lead to a large number of lost features, which is not meaningful as these will easily be preserved even with large compression rates. Thus, both cases are not desirable.

The visual scene is depicted in Fig. 33. The pedestrian walks in a radial direction towards the radar and back to his initial position. Here, very low frequencies have been removed from the original radar data since they are corrupted by the coupling of the antennas within the radar module, which corresponds to a high amplitude within the first meter.

The processed image, which is used as a starting point, is depicted in Fig. 31. The range of the color bar was chosen in a way that the noise floor is easily perceptible. The lamppost is visible in the points at $v = 0$. The pedestrian is represented by a horizontal line indicating his velocity and movement. The horizontal line is due to the fact that a walking human's arms and legs have a very specific micro-Doppler signature featuring many different velocities.

The variations of the noise floor level and the impacts of the different compression algorithms are directly demonstrated on the range-Doppler maps. The settings for the compression algorithm were chosen beforehand to maintain both the highly reflective, static targets as well as the moving pedestrian. Selected range-Doppler maps based on compressed data are depicted in Fig. 35–39. For a better comparison, the dynamic range and the lower limit of the color bars were kept identical
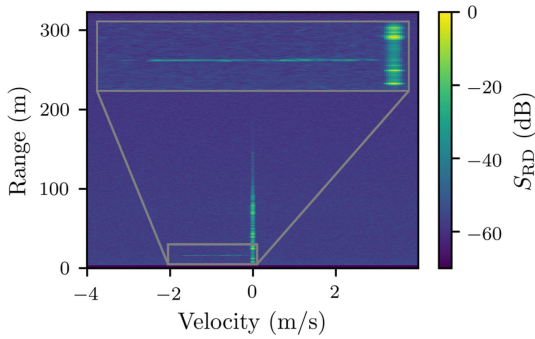
FIGURE 34. Processed reference range-Doppler image of the measurement scenery with a moving pedestrian. The radar faces several obstacles such as a lamp and a container. The high differences in the amplitudes of the static objects (horizontal at v = 0) in comparison to the moving pedestrian (vertical line with v < 0) are easily observable.
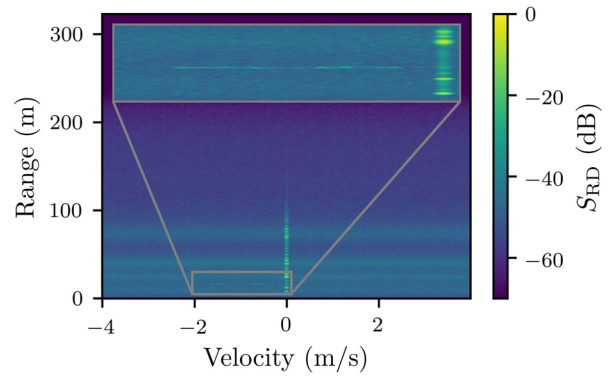

FIGURE 37. Range-Doppler image of the measurement scenery for a compression with Ogg Opus (12 kbit/s). Here, a bandwidth limit as well as strong noise shaping is visible. The compression ratio is 33 for this image.
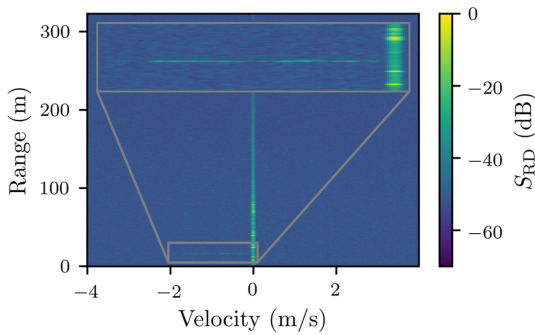

FIGURE 35. Range-Doppler image of the measurement scenery for a quantization with 1 bit. The noise level is significantly increased, but the pedestrian as well as the other targets can still be detected. The compression ratio is 14 for this image.
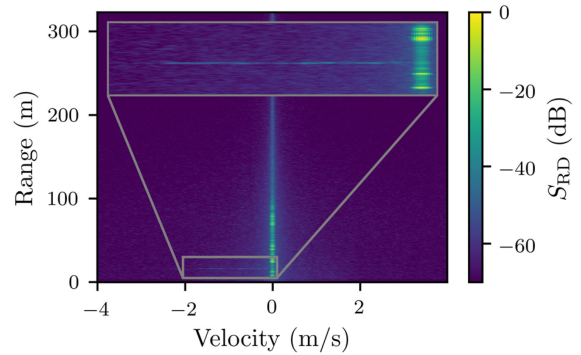

FIGURE 38. Range-Doppler image of the measurement scenery for a compression with HEVC (QP = -14). The leakage of noise around the high amplitude values of the obstacles at a velocity of 0 m/s is directly visible. The compression ratio is 91 for this image.
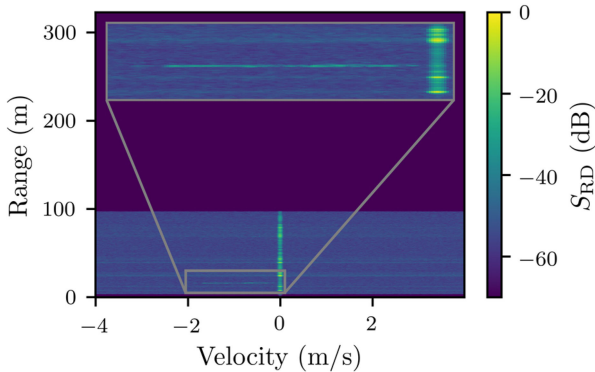

FIGURE 36. Range-Doppler image of the measurement scenery for an AAC compression with 36 kbit/s. A sharp bandwidth limit is clearly visible as well as a slight noise-shaping in the highlighted section. The compression ratio is 21 for this image.
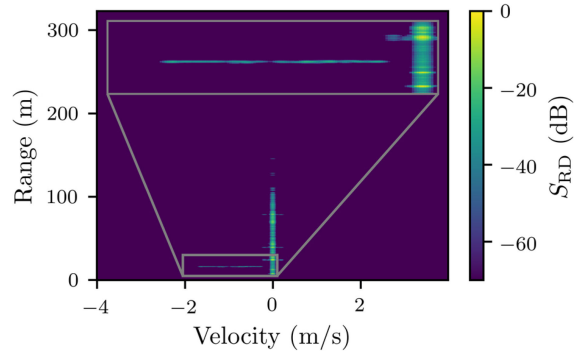

FIGURE 39. Range-Doppler image of the measurement scenery for a DFT-based compression. Obviously, the noise floor was largely removed. The compression ratio is 5900 for this image.

for all figures. However, the tradeoff from tuning the parameters is data integrity against compression ratios. Again, the FLAC algorithm is not displayed as its result is identical to Fig. 34.

We started with the reduced number of bits as the established simplest compression. The results are shown in Fig. 35 for a quantization with only 1 bit. The noise floor increased by approximately 10 dB. However, the targets can still be distinguished.

As seen beforehand, the audio algorithms AAC (Fig. 36) and Ogg Opus (Fig. 37) remove high frequency components

TABLE 3. Median Results for the Measurement Data With the Lowest Settings Shown in Fig. 34–39

Algorithm	Compression Ratio	Rate Saving
Uncompressed	1	0 %
FLAC	2.4	58 %
Quantization	14	92.9 %
AAC	21	95.2 %
OGG	34	97.1 %
HEVC	100	99 %
DFT	5000	99.98 %

abruptly. Furthermore, noise shaping in terms of a smearing of large targets in Doppler dimension is visible, especially for the Ogg Opus codec. Thus, while algorithms preserved the desired data, it should be mentioned that they need to be used cautiously, since data in certain areas were lost.

Meanwhile, the HEVC compression in Fig. 38 transmitted noisy components within small distances to areas with high amplitudes, but struggled to preserve the low amplitude signals of the pedestrian, which highly limited the compression factor.

Next, the DFT algorithm presented in Fig. 39 strictly removed the noise. For this algorithm, the limit had to be set appropriately for the corresponding radar system since it highly influences the noise level and the probability of losing relevant information.

The chosen settings were applied to 20 different images, and the mean values of the compression ratios are depicted in Table 3. As a comparison, the number of range-Doppler data that would fit into one gigabyte is given. Here, the FLAC algorithm achieved the lowest compression because as a consequence of its lossless nature, it needs to preserve the noise in radar signals perfectly. The values used in the real-world sceneries only use about 8 bits (calculated by the original entropy) about 50% of the full range. Combined with the FLAC compression ratio of 1.3 (established in Section V), it reaches a ratio of approximately 2.6.

Quantization is the simplest lossy compression algorithm with the most brute force included here. It features a considerable rate of compression. However, this algorithm is limited by the minimum size of a sample, which is 1 bit, and it is therefore not possible to further reduce the output size. Besides that, the noise level increased steadily, and consequently, it not be used for systems with a lower SNR. The audio codecs achieved considerable good results with compression ratios of 20 to 33. However, they came at the expense of losing high frequency components as well as increased noise levels. Moreover, the video compression algorithm HEVC improved the compression ratio to around 100 at the expense of transmitted noise and, consequently, a lower SNR. Finally, the DFT did not transmit large quantities of noise and increased the ratio further to about 5000, since it performs well for real sceneries with limited regions of interest.

VIII. CONCLUSION

In this paper, the performances of different standard compression algorithms for automotive radar data were evaluated. Audio algorithms, such as AAC and Ogg Opus, have shown limited compression ratios with mixed results. Further, the well-established video codec HEVC showed good results. With this codec, we were able to reach data compression ratios of approximately 100, while still maintaining good visual comparability. A novel approach using a specialized DFT algorithm showed even better results with a compression ratio of around 5000 for real measurement results as presented in Section VII. Of course, lossless compression (e.g., with the FLAC algorithm) also has benefits, but the capabilities are limited for radar data since these signals are often distorted by high noise levels.

Our results showed the possibilities of compressing radar data by high compression factors. Since our results are independent of the deployed radar sensor, these results can be used to start the development of a standardized radar-data protocol. Further, the compression algorithms need to be evaluated for a large variety of different real-world radar systems and scenes. Other applications or different modulation schemes and larger or sparser antenna arrays also need to be tested in real-world applications. Additionally, more research will be needed to develop algorithms for efficient implementations in hardware and software (FPGA, application specific integrated circuits (ASIC), or microprocessors) for embedded applications.

ACKNOWLEDGMENT

REFERENCES

[1] M. Jukl, S. Lacković, and F. Pregernik, "Radar transmitter and two targets simulator for surveilance radar system," in *Proc. Int. Symp. ELMAR*, 2016, pp. 155–159, doi: 10.1109/ELMAR.2016.7731776.

[2] X. Xianlei, M. Zheng, L. Junpeng, and X. Dongshan, "Research on the geological radar antenna for application in full space of mine roadway," in *Proc. 17th Int. Conf. Ground Penetrat. Radar*, 2018, pp. 1–4, doi: 10.1109/ICGPR.2018.8441616.

[3] S. Benchikh, H. Arab and S. O. Tatu, "A novel millimeter wave radar sensor for medical signal detection," in *Proc. IEEE Int. Microw. Biomed. Conf.*, 2018, pp. 142–144, doi: 10.1109/IMBIOC.2018.8428869.

[4] W. Wiesbeck and L. Sit, "Radar 2020: The future of radar systems," in *Proc. Int. Radar Conf.*, 2014, pp. 1–6, doi: 10.1109/RADAR.2014.7060395.

[5] F. Roos, J. Bechter, C. Knill, B. Schweizer and C. Waldschmidt, "Radar sensors for autonomous driving: Modulation schemes and interference mitigation," *IEEE Microw. Mag.*, vol. 20, no. 9, pp. 58–72, Sep. 2019, doi: 10.1109/MMM.2019.2922120.

[6] D. Feng *et al.*, "Deep multi-modal object detection and semantic segmentation for autonomous driving: Datasets, methods, and challenges," *IEEE Trans. Intell. Transp. Syst.*, vol. 22, no. 3, pp. 1341–1360, Mar. 2021, doi: 10.1109/TITS.2020.2972974.

[7] R. Prophet, Y. Jin, J. -C. Fuentes-Michel, A. Deligiannis, I. Weber and M. Vossiek, "CNN based road course estimation on automotive radar data with various gridmaps," in *Proc. IEEE MTT-S Int. Conf. Microw. Intell. Mobility*, 2020, pp. 1–4, doi: 10.1109/ICMIM48759.2020.9299086.

[8] J. Dickmann *et al.*, "Automotive radar the key technology for autonomous driving: From detection and ranging to environmental understanding," in *Proc. IEEE Radar Conf.*, 2016, pp. 1–6, doi: 10.1109/RADAR.2016.7485214.

[9] S. M. Patole, M. Torlak, D. Wang and M. Ali, "Automotive radars: A review of signal processing techniques," *IEEE Signal Process. Mag.*, vol. 34, no. 2, pp. 22–35, Mar. 2017, doi: 10.1109/MSP.2016.2628914.

[10] R. Prophet, H. Stark, M. Hoffmann, C. Sturm and M. Vossiek, "Adaptions for automotive radar based occupancy gridmaps," in *Proc. IEEE MTT-S Int. Conf. Microw. Intell. Mobility*, 2018, pp. 1–4, doi: 10.1109/ICMIM.2018.8443484.

[11] M. Gottinger *et al.*, "Coherent automotive radar networks: The next generation of radar-based imaging and mapping," *IEEE J. Microwaves*, vol. 1, no. 1, pp. 149–163, Jan. 2021, doi: 10.1109/JMW.2020.3034475.

[12] G. Kim, J. Mun and J. Lee, "A Peer-to-Peer interference analysis for automotive chirp sequence radars," *IEEE Trans. Veh. Technol.*, vol. 67, no. 9, pp. 8110–8117, Sep. 2018, doi: 10.1109/TVT.2018.2848898.

[13] B. Lu, X. Zhang, Q. Song, Z. Zhou and J. Wang, "A vehicle based SFCW SAR for differential interferometry," in *Proc. 3rd Int. Asia-Pacific Conf. Synthetic Aperture Radar*, 2011, pp. 1–4.

[14] S. H. Dokhanchi, M. R. B. Shankar, T. Stifter and B. Ottersten, "OFDM-based automotive joint radar-communication system," in *Proc. IEEE Radar Conf.*, 2018, pp. 0902–0907, doi: 10.1109/RADAR.2018.8378680.

[15] W. D. Jones, "Keeping cars from crashing," *IEEE Spectr.*, vol. 38, no. 9, pp. 40–45, Sep. 2001, doi: 10.1109/6.946636.

[16] J. W. Campbell, "The lognormal distribution as a model for bio-optical variability in the sea," *J. Geophys. Res., Oceans*, vol. 100, no. C7, pp. 13237–13254, 1995, doi: 10.1029/95JC00458.

[17] D. K. Barton, *Radar Equations for Modern Radar*. Norwood, MA, USA: Artech House, 2013, pp. 2–3.

[18] INRAS, "Produkte - Radarbook (obsolete) - HF-frontends." 2015. Accessed: Jun. 14, 2021. [Online]. Available: http://www.inras.at/produkte/radarbook/hf-frontends.html

[19] A. Meta, P. Hoogeboom and L. P. Ligthart, "Signal processing for FMCW SAR," *IEEE Trans. Geosci. Remote Sens.*, vol. 45, no. 11, pp. 3519–3532, Nov. 2007, doi: 10.1109/TGRS.2007.906140.

[20] Y. L. Sit, C. Sturm and T. Zwick, "Doppler estimation in an OFDM joint radar and communication system," in *Proc. German Microw. Conf.*, 2011, pp. 1–4.

[21] M. Umehira, Y. Watanabe, X. Wang, S. Takeda and H. Kuroda, "Inter-radar interference in automotive FMCW radars and its mitigation challenges," in *Proc. IEEE Int. Symp. Radio-Freq. Integrat. Technol.*, 2020, pp. 220–222, doi: 10.1109/RFIT49453.2020.9226222.

[22] Zhenyu Ding, Yanping Wang, Weixian Tan and Wen Hong, "Experimental verification of stepped frequency continuous wave ground-based SAR," in *Proc. IET Int. Radar Conf.*, 2013, pp. 1–5, doi: 10.1049/cp.2013.0195.

[23] A. Bourdoux, U. Ahmad, D. Guermandi, S. Brebels, A. Dewilde and W. Van Thillo, "PMCW waveform and MIMO technique for a 79 GHz CMOS automotive radar," in *Proc. IEEE Radar Conf.*, 2016, pp. 1–5, doi: 10.1109/RADAR.2016.7485114.

[24] L. Brennan, "Angular accuracy of a phased array radar," *IRE Trans. Antennas Propag.*, vol. 9, no. 3, pp. 268–275, May 1961, doi: 10.1109/TAP.1961.1145000.

[25] B. Elias, "Radar theoretical study: Minimum detection range and maximum signal to noise ratio (SNR) equation by using MATLAB simulation program," *Amer. J. Modern Phys.*, vol. 2, pp. 234–241, Jan. 2013.

[26] L. Su, H. S. Wu and C. C. Tzuang, "2-D FFT and time-frequency analysis techniques for multi-target recognition of FMCW radar signal," in *Proc. Asia-Pacific Microw. Conf.*, 2011, pp. 1390–1393.

[27] F. M. Remley, J. F. X. Browne, and S. N. Baron, "Broadcasting, cable television, and recording system standards," in *Reference Data for Engineers*, 9th ed., W. M. Middleton and M. E. Van Valkenburg, Eds. Woburn, MA, USA: Newnes, 2002, ch. 35, pp. 35–31, doi: 10.1016/B978-075067291-7/50037-6.

[28] A. Horé and D. Ziou, "Image quality metrics: PSNR vs. SSIM," in *Proc. 20th Int. Conf. Pattern Recognit.*, 2010, pp. 2366–2369, doi: 10.1109/ICPR.2010.579.

[29] N. M. Suaib, M. H. Marhaban, M. I. Saripan and S. A. Ahmad, "Performance evaluation of feature detection and feature matching for stereo visual odometry using SIFT and SURF," in *Proc. IEEE Region Symp.*, 2014, pp. 200–203, doi: 10.1109/TENCONSpring.2014.6863025.

[30] M. Kronauge and H. Rohling, "Fast two-dimensional CFAR procedure," *IEEE Trans. Aerosp. Electron. Syst.*, vol. 49, no. 3, pp. 1817–1823, Jul. 2013, doi: 10.1109/TAES.2013.6558022.

[31] H. Ye and E. McCreath, "FLAC decoding using GPU acceleration," in *Proc. IEEE Int. Conf. Parallel Distrib. Process. Appl., Ubiquitous Comput. Commun., Big Data Cloud Comput., Social Comput. Netw., Sustain. Comput. Commun.*, 2018, pp. 155–162, doi: 10.1109/BDCloud.2018.00035.

[32] FFMPEG Software, "FFmpeg v4.4," 2021. Accessed: Mar. 08, 2021. [Online]. Available: https://ffmpeg.org

[33] K. Takagi, S. Miyaji, S. Sakazawa and Y. Takishima, "Conversion of MP3 to AAC in the compressed domain," in *Proc. IEEE Workshop Multimedia Signal Process.*, 2006, pp. 132–135, doi: 10.1109/MMSP.2006.285283.

[34] S. D. You and P. Lai, "On the efficiency difference between range and huffman coding on CELT layer of opus audio coder," in *Proc. IEEE Int. Conf. Consum. Electron.-Taiwan*, 2018, pp. 1–2, doi: 10.1109/ICCE-China.2018.8448721.

[35] GitLab, "Joint collaborative team on video coding (JCT-VC)," 2021. Accessed: May 17, 2021. [Online]. Available: https://vcgit.hhi.fraunhofer.de/jvet/HM

[36] ITU-T and ISO/IEC JTC 1/SC29/WG 11(MPEG), "High efficiency video coding, document ITU-T rec. H.265 and ISO/IEC 23008-2," Apr. 2013. Accessed: Oct. 26, 2021. [Online]. Available: http://handle.itu.int/11.1002/1000/11830-en

[37] F. Bossen, *Common Test Conditions and Software Reference Configurations, Document JCTVC-L1100*. Geneva, Switzerland: ITU-T VCEG and ISO/IEC MPEG (JCT-VC), 2013.

[38] X. Zhao and B. Li, "Implementation of the LZMA compression algorithm on FPGA," in *Proc. Int. Conf. Electron Devices Solid-State Circuits*, 2017, pp. 1–2, doi: 10.1109/EDSSC.2017.8126506.

[39] M. A. Richards, "The discrete-time fourier transform and discrete fourier transform of windowed stationary white noise," Nov. 2013. [Online]. Available: https://radarsp.weebly.com/uploads/2/1/4/7/21471216/dft_of_noise.pdf

[40] I. Amidror, *Mastering the Discrete Fourier Transform in One, Two or Several Dimensions: Pitfalls and Artifacts*, vol. 43. London, U.K.: Springer, 2013, pp. 143–173, doi: 10.1007/978-1-4471-5167-8.

[41] M. A. Richards, *Fundamentals of Radar Signal Processing*, 2nd ed. New York, NY, USA: McGraw-Hill Education, 2014, pp. 18–24.

[42] B. Rivet, L. Girin and C. Jutten, "Log-Rayleigh distribution: A simple and efficient statistical representation of log-spectral coefficients," *IEEE Trans. Audio, Speech, Lang. Process.*, vol. 15, no. 3, pp. 796–802, Mar. 2007, doi: 10.1109/TASL.2006.885922.

[43] C. E. Shannon, "A mathematical theory of communication," *Bell System Tech. J.*, vol. 27, no. 3, pp. 379–423, Jul. 1948, doi: 10.1002/j.1538-7305.1948.tb01338.x.

[44] "Symeo datasheet AVR-QDM-110." Accessed: Jul. 07, 2021. [Online]. Available: https://www.symeo.com/cms/upload/pdf/en/DataSheets/DOC.DBL.000443.LATEST.Symeo_Datasheet_AVR-QDM-110.pdf

GEORG KÖRNER received the B.Eng. degree in electrical engineering from the TH Nürnberg Georg-Simon-Ohm, Nuremberg, Germany, in 2015, and the M.Sc. degree in information and communication technologies from the Friedrich Alexander Universität Erlangen-Nürnberg (FAU), Erlangen, Germany, in 2017. From 2014 to 2016, he was a Research Assistant with Siemens AG in the field of fiber-optic photonics. After graduation, he joined the Institute of Microwaves and Photonics (LHFT) with FAU in 2017, where he is currently working toward the Ph.D. His research interests include radar signal processing, radar target simulation, and radar hardware.

MARCEL HOFFMANN (Student Member, IEEE) was born in Witten, Germany, in 1994. He received the B.Sc. and M.Sc. degrees in electrical engineering from the Friedrich-Alexander University Erlangen-Nürnberg, Erlangen, Germany, in 2016 and 2018, respectively. In 2018, he joined the Institute of Microwaves and Photonics (LHFT) with the Friedrich-Alexander University Erlangen-Nürnberg, where he is currently working toward the Ph.D. His research interests include radar signal processing and automotive radar applications, including new SAR and SLAM approaches.

PATRICK STIEF received the B.Sc. and M.Sc. degrees in electrical engineering from Friedrich-Alexander-Universität Erlangen-Nürnberg (FAU), Erlangen, Germany, in 2016 and 2018, respectively, where he is currently working toward the Ph.D. degree. In 2019, he joined the Institute of Microwaves and Photonics (LHFT), FAU. His current research interests include radar signal processing, radar target simulation, radar imaging, and machine learning-based radars.

MENGYU ZHANG received the bachelor's degree in electrical engineering and automation from the Nanjing University of Science and Technology, Jiangsu, China, in 2014 and the master's degree in electrical engineering from the Friedrich-Alexander Universität Erlangen-Nürnberg, Erlangen, Germany, in 2020. In 2021, she joined the Institute of Microwaves and Photonics (LHFT), FAU, Erlangen, Germany. Her research interests include automotive radar signal processing and machine learning techniques.

RAINER RÜCKERT received the B.Eng. degree in electrical engineering and information technology and the M.Eng. degree in electronic and mechatronic systems from the Technische Hochschule Nürnberg Georg Simon Ohm, Nuremberg, Germany, in 2017 and 2019, respectively. From 2015 to 2018, as part of his cooperative education, he worked with Continental AG in the field of automotive control systems. In 2018, he joined the Institute of Microwaves and Photonics (LHFT) with the Friedrich-Alexander-Universität Erlangen-Nürnberg, Erlangen, Germany. His research interests include radar signal processing and radar hardware.

CHRISTIAN HERGLOTZ (Member, IEEE) received the Dipl.-Ing. in electrical engineering and information technology in 2011 and the Dipl.-Wirt. Ing. in business administration and economics in 2012, both from Rheinisch-Westfälische Technische Hochschule (RWTH), Aachen University, Germany. Since 2012, he has been a Research Scientist with the Chair of Multimedia Communications and Signal Processing, Friedrich-Alexander Universität Erlangen-Nürnberg (FAU), Germany, where he received the Dr.-Ing. degree in 2017. In 2018 and 2019, he worked as a PostDoc-Fellow with École de technologie supérieure in collaboration with Summit Tech Multimedia, Montréal, Canada on energy efficient VR technologies. Since 2019, he has been with FAU as a Senior Scientist. Since 2020, he has been with the Visual Signal Processing and Communications (VSPC) Technical Committee of IEEE Circuits and Systems Society. He is a Guest Editor for the *Open Journal on Circuits and Systems* (OJCAS). His current research interests include energy efficient video communications and video coding.

ANDRÉ KAUP (Fellow, IEEE) received the Dipl.-Ing. and Dr.-Ing. degrees in electrical engineering from RWTH Aachen University, Aachen, Germany, in 1989 and 1995, respectively. He joined Siemens Corporate Technology, Munich, Germany, in 1995, and became the Head of the Mobile Applications and Services Group in 1999. Since 2001, he has been a Full Professor and the Head of the Chair of Multimedia Communications and Signal Processing with Friedrich-Alexander University Erlangen-Nuremberg (FAU), Germany. From 2005 to 2007, he was Vice Speaker of the DFG Collaborative Research Center 603. From 2015 to 2017, he was the Head of the Department of Electrical Engineering and the Vice Dean of the Faculty of Engineering with FAU. He has authored around 400 journal and conference papers and has over 120 patents granted or pending. His research interests include image and video signal processing and coding, and multimedia communication. Dr. Kaup is a member of the IEEE Multimedia Signal Processing Technical Committee and the Scientific Advisory Board of the German VDE/ITG. In 2018, he was elected as a Full Member with the Bavarian Academy of Sciences. He was a Siemens Inventor of the Year 1998 and received the 1999 ITG Award and several IEEE best paper awards. His group won the Grand Video Compression Challenge from the Picture Coding Symposium 2013. The Faculty of Engineering with FAU and the State of Bavaria honored him with teaching awards, in 2015 and 2020, respectively. He was as an Associate Editor for IEEE TRANSACTIONS ON CIRCUITS AND SYSTEMS FOR VIDEO TECHNOLOGY. He was a Guest Editor for IEEE JOURNAL OF SELECTED TOPICS IN SIGNAL PROCESSING.

MARTIN VOSSIEK (Fellow, IEEE) received the Ph.D. degree from Ruhr-Universität Bochum, Bochum, Germany, in 1996. In 1996, he joined Siemens Corporate Technology, Munich, Germany, where he was the Head of the Microwave Systems Group, from 2000 to 2003. Since 2003, he has been a Full Professor with Clausthal University, Clausthal-Zellerfeld, Germany. Since 2011, he has been the Chair of the Institute of Microwaves and Photonics (LHFT), Friedrich-Alexander-Universität Erlangen-Nürnberg (FAU), Erlangen, Germany. He has authored or coauthored more than 300 articles. His research has led to more than 90 granted patents. His current research interests include radar, transponder, RF identification, communication, and wireless locating systems. Martin Vossiek is a member of the German National Academy of Science and Engineering (acatech) and of the German research foundation (DFG) review board. He is a member of the German IEEE Microwave Theory and Techniques (MTT)/Antennas and Propagation (AP) Chapter Executive Board and a member of the IEEE MTT Technical Committees MTT-24 Microwave/mm-wave Radar, Sensing, and Array Systems; MTT-27 Connected and Autonomous Systems (as founding chair); MTT-29 Microwave Aerospace Systems. He is also on the advisory board of the IEEE CRFID Technical Committee on Motion Capture & Localization. Martin Vossiek has received more than ten best paper prices and several other awards. For example, he was awarded the 2019 Microwave Application Award from IEEE MTT Society (MTT-S) for Pioneering Research in Wireless Local Positioning Systems. Dr. Vossiek has been a member of organizing committees and technical program committees for many international conferences and he was on the Review Boards for numerous technical journals. From 2013 to 2019, he was an Associate Editor for IEEE TRANSACTIONS ON MICROWAVE THEORY AND TECHNIQUES.